ACS OMEGA

http://pubs.acs.org/journal/acsodf

Article

24% Efficient, Simple ZnSe/Sb_2Se_3 Heterojunction Solar Cell: An Analysis of PV Characteristics and Defects

Raman Kumari, Mamta Mamta, Rahul Kumar, Yogesh Singh, and Vidya Nand Singh*

Cite This: *ACS Omega* 2023, 8, 1632−1642

Read Online

ACCESS | Metrics & More | Article Recommendations | Supporting Information

ABSTRACT: In this work, a new wide-band-gap n-type buffer layer, ZnSe, has been proposed and investigated for an antimony selenide (Sb_2Se_3)-based thin-film solar cell. The study aims to boost the Sb_2Se_3-based solar cell's performance by incorporating a cheap, widely accessible ZnSe buffer layer into the solar cell structure as a replacement for the CdS layer. Solar Cell Capacitance Simulator in One Dimension (SCAPS-1D) simulation software is used to thoroughly analyze the photovoltaic parameters of the heterojunction structure ZnSe/Sb_2Se_3. It includes open circuit voltage (V_{OC}), short-circuit current density (J_{SC}), fill factor (FF), power conversion efficiency (PCE), and external quantum efficiency (EQE). The absorber layer (Sb_2Se_3) thickness is adjusted from 0.5 to 3.0 μm to perfect the device. In addition, the influence of cell resistances, radiative recombination coefficient, acceptor and donor defect concentration in the Sb_2Se_3 layer, and interface defects of the ZnSe/Sb_2Se_3 layer on overall device performance are investigated. The ZnSe buffer layer and the Sb_2Se_3 absorber layer are designed to have optimal thicknesses of 100 nm and 1.5 μm, respectively. The proposed device's efficiency with optimized parameters is calculated to be 24%. According to the simulation results, it is possible to build Sb_2Se_3-based thin-film solar devices at a low cost and with high efficiency by incorporating ZnSe as an electron transport layer.

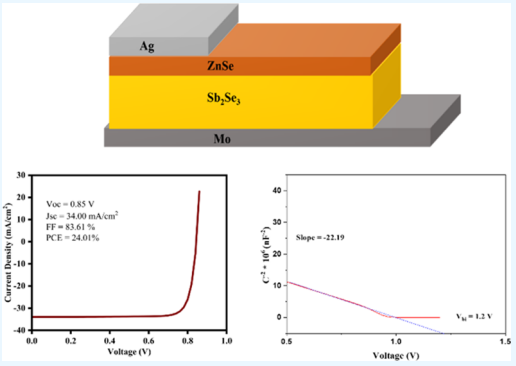

1. INTRODUCTION

In thin-film solar cells, high bulk lifespan, effective carrier collection efficiency, sufficient photon absorption, and superior junction interface contribute to high device performance. Sb_2Se_3 has demonstrated excellent potential as an absorber material in thin-film solar cell (TFSC) technology.[1−4] It is a binary compound having less-toxic and earth-rich elements. It has decent carrier mobility (electron mobility of >16.9 $cm^2\ V^{-1}\ s^{-1}$ and hole mobility of >0.69 $cm^2\ V^{-1}\ s^{-1}$),[5] a high absorption coefficient over the visible spectrum (>10^5 cm^{-1}), and a band gap of 1.2 eV.[1] In 2009, Messina et al. achieved 0.66% power conversion efficiency (PCE) with CdS as a buffer layer.[6] After 5 years, in 2014, Zhou et al. and Choi et al. achieved 2.26 and 3.21% power conversion efficiency (PCE) with TiO_2 as a buffer layer, respectively.[2,7] Wang et al. and Chen et al. gained 5.93 and 6.5% PCEs with ZnO and CdS as buffer layers, respectively, in 2017.[3,4] In 2018, Wen et al. achieved 7.6% efficiency using a vapor-transport-deposited Sb_2Se_3 film and a CdS buffer layer.[8] The highest efficiency obtained by Sb_2Se_3 thin-film solar cells was 9.2% in 2019, with CdS as a buffer layer.[1] Many simulations were done to determine the theoretical PCE of Sb_2Se_3 solar cells. Mamta et al. achieved 27.84% efficiency for the Sb_2Se_3/CdS/ZnO solar device with a CdS buffer layer using SCAPS-1D.[9] Ahmed et al. achieved 29.35% efficiency in Al/FTO/CdS/Sb_2Se_3/$BaSi_2$/Mo solar devices using SCAPS-1D.[10] Baig et al. used In_2S_3 as a buffer layer and achieved 13.20% efficiency using SCAPS-1D.[11]

Defects in the Sb_2Se_3 layer lead to carrier recombination and low device performance. The dangling bonds at grain boundaries act as recombination centers in a 3D crystal structure.[12] Intrinsic point defects such as substitution/antisite (Sb_{Se}, Se_{Sb}), vacancies (V_{Se}, V_{Sb}), and interstitials (Se_i), which can be donor/acceptor/amphoteric, could act as both hole and electron traps and reduce the lifespan of the minority carrier lifetime and the solar cell performance.[13]

An ideal buffer layer should satisfy the fundamental criteria of having good carrier mobility, high electrical conductivity, and an appropriate energy band alignment with minimum conduction band offset (CBO).[14] In Sb_2Se_3 TFSC, CdS is a commonly used buffer layer. The primary issue with the CdS thin film is its toxicity, which raises concerns for plants, the environment, and human health and is generally classified as a carcinogen.[15−17] Besides its toxicity, Cd and S diffuse into the Sb_2Se_3 layer, which decreases the device performance, and CdS has a high lattice mismatch with the Sb_2Se_3 layer. Because of its narrow band gap of 2.4 eV, the CdS layer parasitically absorbs

Received: November 9, 2022
Accepted: December 13, 2022
Published: December 21, 2022

https://doi.org/10.1021/acsomega.2c07211
ACS Omega 2023, 8, 1632−1642

blue light, which causes photocurrent and conversion loss.[18,19] The wide-band-gap buffer material provides high UV absorption and optical transparency in visible and IR regions.[3,20] ZnSe having an energy gap of 2.7 eV is a direct wide-energy-gap semiconductor with a higher energy gap than CdS. It has permeability through a broad range of the visible spectrum and has a significant nonlinear optical coefficient value.[21] ZnSe can be synthesized by thermal evaporation, spray pyrolysis, chemical bath deposition, electrodeposition, etc.[22−25]

In this work, the ZnSe/Sb_2Se_3 device analysis is performed by tuning the thickness of absorber and buffer layers, radiative recombination coefficient, shallow acceptor density, absorber defects, interface defect density, back contact work function, and series and shunt resistance with the aid of SCAPS-1D software. The performance of a solar cell is optimized by considering each of these factors. The many junction properties, including current density−voltage (J−V), built-in voltage by the Mott−Schottky plot, and energy band formation, have also been simulated.

2. DEVICE STRUCTURE AND PARAMETERS OF MATERIALS USED IN MODELING

2.1. Device Structure. The solar device structure is Mo/Sb_2Se_3/ZnSe/Ag, as shown in Figure 1, where Sb_2Se_3 is the absorber layer, ZnSe is the buffer layer, and Mo and Ag are the rear and front contacts, respectively.

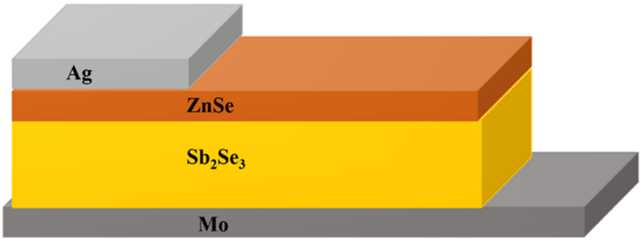

Figure 1. Schematic of the proposed Mo/Sb_2Se_3/ZnSe/Ag solar cell.

2.2. Solar Cell Modeling Parameters. The performance of TFSCs can be investigated using a variety of applications, including COMSOL,[26] SILVACO ATLAS,[27] SCAPS,[28] wxAMPS,[29] and AMPS.[30] SCAPS is a 1D (Version 3.3.07) solar cell simulation software created by the Department of Electronics and Information Systems at Gent University in Belgium. It was utilized in the current study to model the capability of solar cells and their many deciding parameters. This software has several benefits, including the potential to execute performance analysis across up to seven levels, in-depth and batch analyses, and simple results to understand and analyze.[31] Three fundamental equations—Poisson's equation, the carrier continuity equation, and the drift-diffusion equation—forming the foundation of the theoretical calculation are as follows

$$\frac{\partial^2\psi}{\partial x^2} = \frac{q}{\varepsilon}(n - p) \tag{1}$$

$$\frac{\partial n}{\partial t} = \frac{1}{q}\frac{\partial J_n}{\partial x} + (G - R), \quad \frac{\partial p}{\partial t} = \frac{1}{q}\frac{\partial J_p}{\partial x} + (G - R) \tag{2}$$

$$J_n = qD_n\frac{\partial n}{\partial x} - q\mu_n n\frac{\partial \varphi}{\partial x}, \quad J_p = qD_p\frac{\partial p}{\partial x} - q\mu_p p\frac{\partial \varphi}{\partial x} \tag{3}$$

where q is the charge on electrons, p is the concentration of holes, ε is the dielectric constant, n is the concentration of electrons, ϕ is the electric potential, R is the carrier recombination rate, G is the carrier generation rate, and J_p is the current density due to holes. J_n is the current density due to electrons. D_n and D_p are coefficients of electron and hole diffusion, respectively, while μ_n and μ_p are the mobilities of electrons and holes, respectively.

Each layer of the structure must contain several material parameters for SCAPS-1D software to simulate device design. The material and interface parameters used for the simulation analysis are shown in Tables 1 and 2, respectively. These parameters were based on the literature.[32,33] The simulation was done under AM 1.5 G, 1000 W m^{-2} illumination intensity, at 300 K. For the absorber and buffer layers, thermal velocity was taken as 10^7 cm s^{-1}.

Table 1. Material Parameters of the n-ZnSe/p-Sb_2Se_3 Solar Cell Used in the Simulation[a]

parameters	p-Sb_2Se_3	n-ZnSe
thickness (μm)	0.5−3.0	0.1
band gap (eV)	1.2	2.7
E_A (eV)	4.04	4.09
ε (relative)	18	10
CB DOS (cm^{-3})	2.4×10^{18}	1.5×10^{18}
VB DOS (cm^{-3})	1.8×10^{19}	1.8×10^{19}
electron thermal velocity (cm s^{-1})	1×10^7	1×10^7
hole thermal velocity (cm s^{-1})	1×10^7	1×10^7
μ_n(cm^2 V^{-1} s^{-1})	15	50
μ_p(cm^2 V^{-1} s^{-1})	5.1	20
N_D (cm^{-3})	0	1×10^{18}
N_A (cm^{-3})	1×10^{13}	0
type of defect	neutral	acceptor
capture cross section of electrons (cm^2)	1×10^{-15}	1×10^{-15}
capture cross section of holes (cm^2)	1×10^{-17}	1×10^{-15}
energetic distribution	Gaussian	single
reference for the defect energy level, E_t	above E_V	above E_V
energy level with respect to a reference (eV)	0.6	1.350
characteristic energy (eV)	0.1	0.1
N_t total (cm^{-3})	1×10^{14}	1×10^{13}

[a] E_A is the electron affinity, ε is the dielectric permittivity, CB DOS is the conduction band density of states, VB DOS is the valence band density of states, μ_n is the electron mobility, μ_p is the hole mobility, N_D is the shallow uniform donor density, N_A is the shallow uniform acceptor density, E_V is the valence band maximum, and N_t is the total defect density.

Table 2. Interface Parameters of the n-ZnSe/p-Sb_2Se_3 Layer

parameters	ZnSe/Sb_2Se_3
type of defect	neutral
capture cross section of electrons (cm^2)	1×10^{-19}
capture cross section of holes (cm^2)	1×10^{-19}
energetic distribution	single
reference for the defect energy level, E_t	above the highest E_V
energy level with respect to a reference (eV)	0.6
characteristic energy (eV)	0.1
total density	1×10^{10}

https://doi.org/10.1021/acsomega.2c07211
ACS Omega 2023, 8, 1632−1642

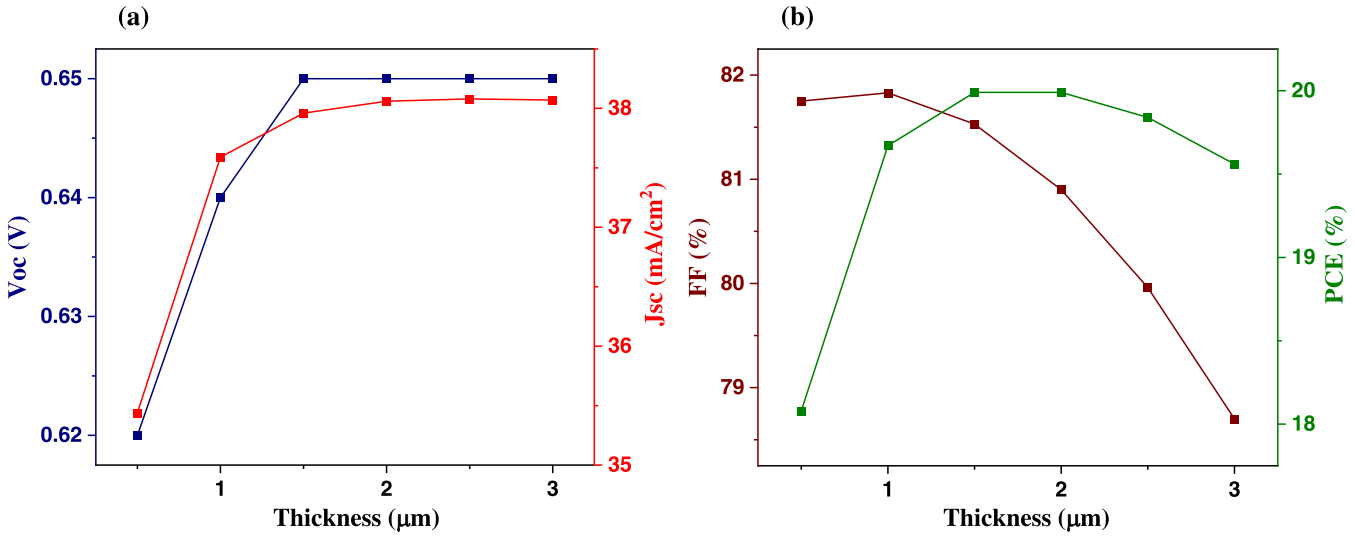

Figure 2. Variation of (a) V_{OC} and J_{SC} and (b) FF and PCE as a function of Sb_2Se_3 absorber layer thickness.

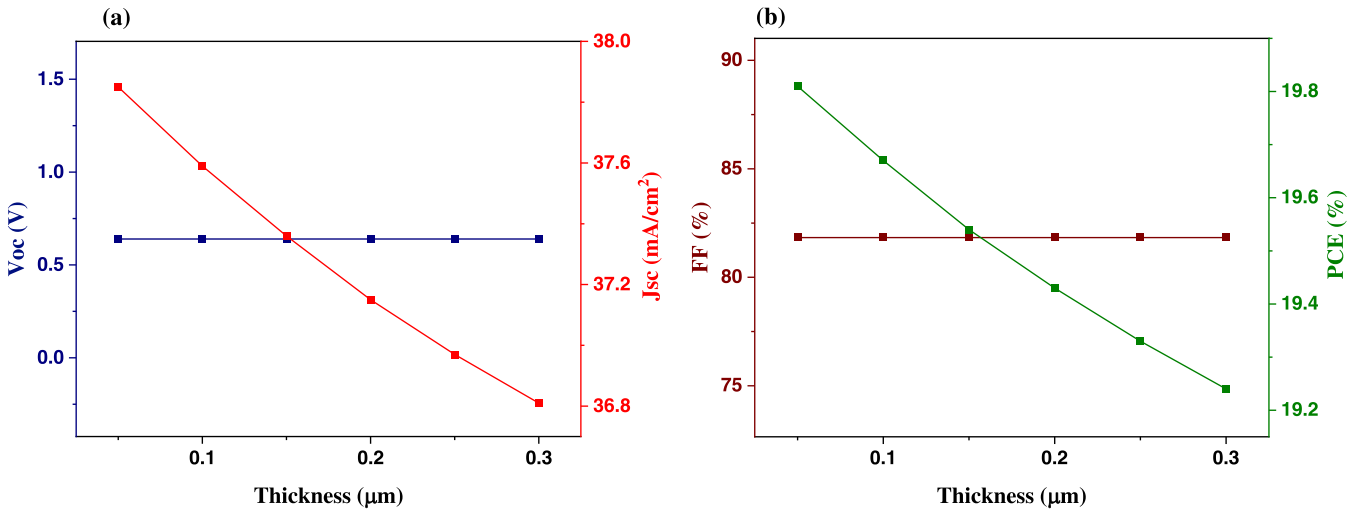

Figure 3. Variation of (a) V_{OC} and J_{SC} and (b) FF and PCE as a function of ZnSe buffer layer thickness.

3. RESULTS AND DISCUSSION

The prime goal of this investigation is to examine the results of varying numerous absorber (Sb_2Se_3) and buffer (ZnSe) layer parameters on solar device photoconversion efficiency.

3.1. Influence of the Varying Absorber Layer (Sb_2Se_3) and Buffer Layer (ZnSe) Thicknesses on Device Performance. The effect of varying the thickness of the Sb_2Se_3 and ZnSe layers on V_{OC}, J_{SC}, fill factor (FF), and PCE is studied in this simulation. The absorber layer thickness is varied in the range from 0.5 to 3.0 μm. It can be seen from Figure 2a that V_{OC} extends to an optimal value of 0.65 V (Table S1) at a thickness of 1.5 μm and remains constant when the thickness is further increased. In contrast, J_{SC} first increases to a value of 38 mA cm^{-2} at 2.0 μm and remains almost constant when Sb_2Se_3 thickness is increased. The saturation of J_{SC} occurs with an increase in absorber thickness because of an increase in the carrier recombination rate with the rate of carrier production.[5] The saturation of V_{OC} occurs because the absorber is thick enough to absorb nearly all incident light, which strengthens the electric field of the p−n junction. It probably reaches a plateau because of the nonradiative losses linked to point defect, carrier lifetime, and interface recombination.

Figure 2b shows that FF increases to 81.83% at 1.0 μm thickness and then decreases when the thickness of the Sb_2Se_3 layer is further increased. In contrast, the PCE value increases to 19.99% at 1.5 μm (Table S2) and then decreases. FF represents the ratio of maximum power output to V_{OC} and J_{SC}, i.e., $FF = \frac{P_{max}}{V_{OC} J_{SC}}$, and PCE represents the ratio of maximum power to incident light, i.e., $PCE = \frac{V_{OC} J_{SC} FF}{I_{in}}$. An increase in the values of J_{SC} and V_{OC} at lower thickness leads to an increase in FF. Still, at higher absorption layer thickness, the depletion is accelerated and the internal resistance increases, decreasing the fill factor. The PCE of a solar cell depends on light absorption and carrier transport. At low absorber layer thickness, light absorption determines the PCE, as a carrier having high diffusion length than thickness can reach the electrode efficiently. At more increased thickness, carrier transport dominates, as light absorption becomes saturated. Thus, the optimum thickness value of Sb_2Se_3, i.e., the absorber layer, is taken as 1.5 μm.

https://doi.org/10.1021/acsomega.2c07211
ACS Omega 2023, 8, 1632−1642

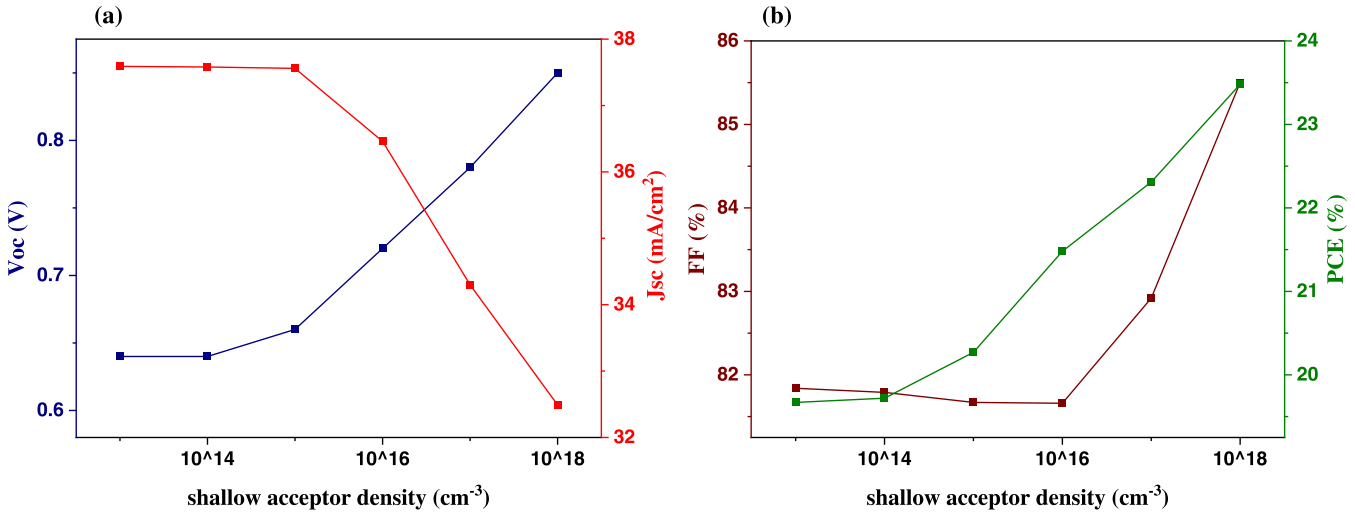

Figure 4. Variation of (a) V_{OC} and J_{SC} and (b) FF and PCE as a function of shallow acceptor doping density.

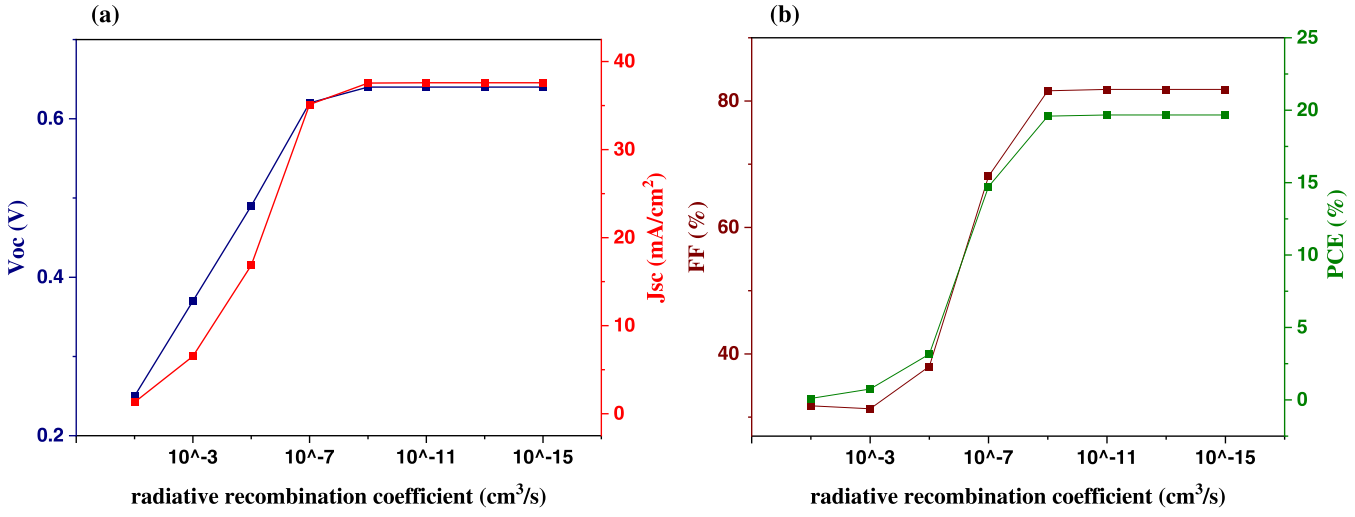

Figure 5. Variation of (a) V_{OC} and J_{SC} and (b) FF and PCE with RRC.

The buffer layer improves the device's performance by charge extraction and collection. In this device, ZnSe is used as a buffer layer, and the influence of varying the thickness on photovoltaic parameters is studied. The thickness value is varied from 50 to 300 nm. From Figure 3a,b, it is perceived that on increasing the thickness of the buffer layer, V_{OC} and FF remain constant, whereas J_{SC} and PCE decrease to 6.81 mA cm^{-2} and 19.24%, respectively. A thick buffer layer will absorb more photons, lowering efficiency, since it prevents them from reaching the absorber layer. It causes a decrease in J_{SC} and PCE. A very thin buffer layer leads to a high leakage current.[34] Thus, the optimal thickness value of the ZnSe buffer layer is 0.1 μm.

3.2. Influence of Varying Shallow Acceptor Doping Densities of the Absorber Layer (Sb_2Se_3) on Device Performance. Acceptor density is a crucial parameter for regulating the solar cell's performance. In this study, the acceptor density changes from 10^{13} to 10^{18} cm^{-3}. From Figure 4a, it can be observed that V_{OC} increases with increases in doping density, whereas J_{SC} decreases. From Figure 4b, FF and PCE increase to 85.5 and 23.5% (Table S3), respectively. The decrease in the value of J_{SC} is due to increased recombination in bulk. V_{OC} and PCE increase with the increase in doping density, whereas FF slightly decreases to 10^{16} cm^{-3} and increases further with an increase in doping concentration. So, the optimal acceptor density is determined to be 10^{18} cm^{-3}. The excessive doping density above 10^{18} cm^{-3} disrupts the crystal structure by forming a shunt path in the solar cell, thereby decreasing efficiency.

3.3. Influence of Varying Radiative Recombination Coefficients. Radiative recombination is the process of direct transition of an electron from the conduction band (CB) to the valence band (VB), and a photon (excess energy) is released. The following expression gives the radiative recombination coefficient

$$R_{rad} = B(np - n_i^2) \quad (4)$$

where B is the radiative recombination coefficient (RRC), np is the concentration of electron−hole in trap states, and n_i is the intrinsic carrier concentration. Recombination is the primary obstruction in creating high-efficiency solar cells.

In this study, the value of RRC is changed in the range of 10^{-1}−10^{-15} cm^3 s^{-1}. Figure 5a,b shows that the maximum values of V_{OC}, J_{SC}, FF, and efficiency are achieved when RRC is 10^{-9} cm^3 s^{-1} and remain constant (Table S4) for values lower

https://doi.org/10.1021/acsomega.2c07211
ACS Omega 2023, 8, 1632−1642

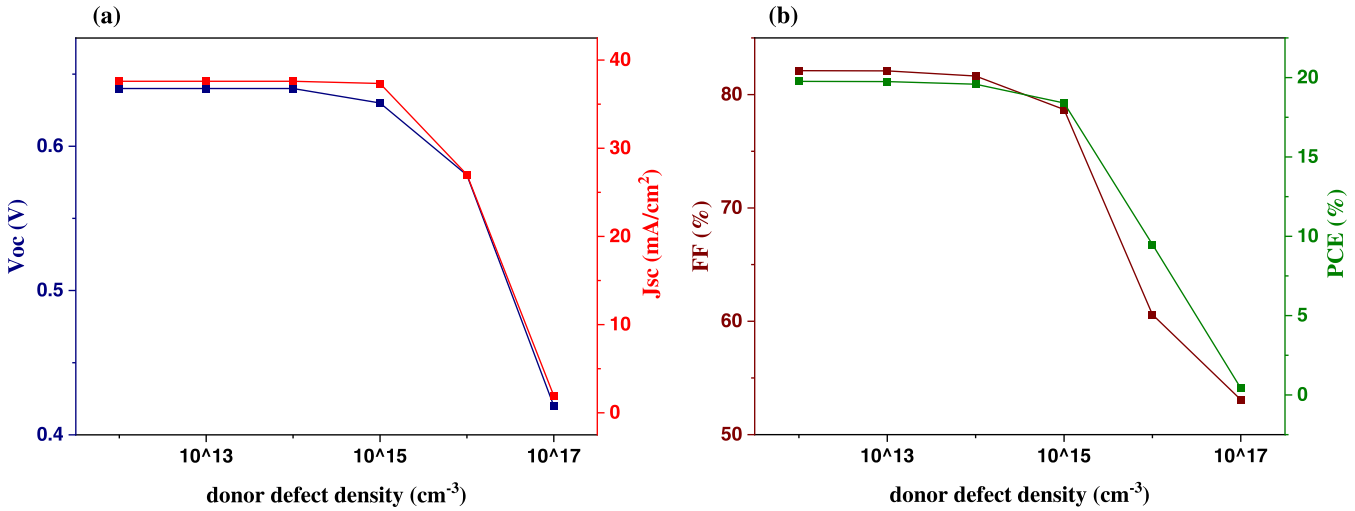

Figure 6. Variation of (a) V_{OC} and J_{SC} and (b) FF and PCE as a function of donor defect density in the absorber layer.

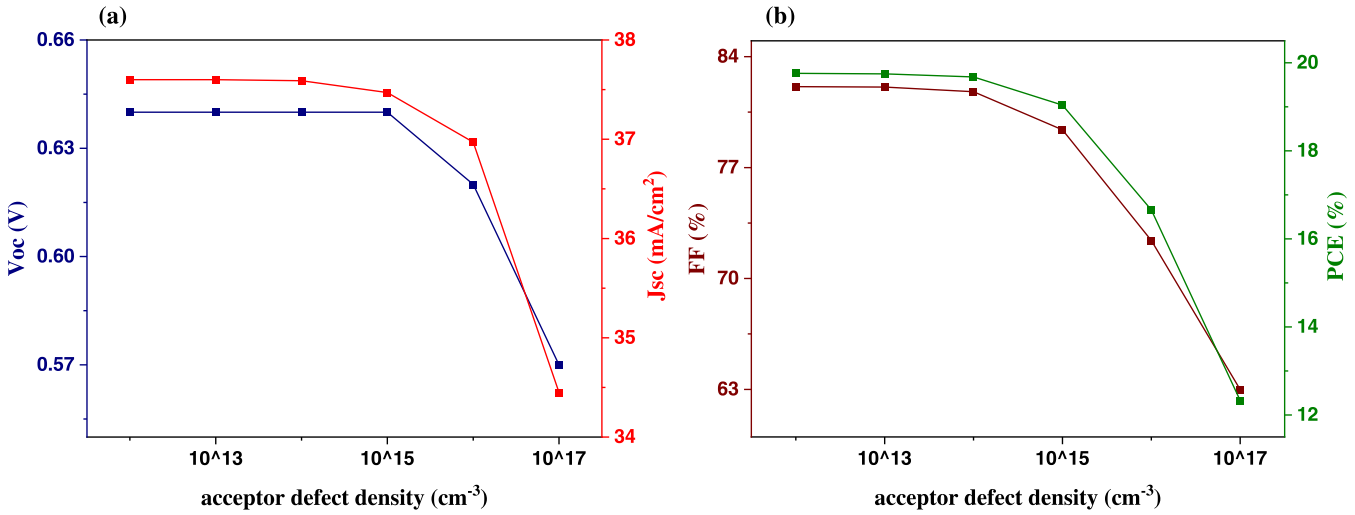

Figure 7. Variation of (a) V_{OC} and J_{SC} and (b) FF and PCE as a function of acceptor defect density in the absorber layer.

than that. The optimal value at which the maximum value of all of the parameters is obtained is 10^{-11} cm^3 s^{-1}.

3.4. Influence of Varying Total Defect Densities in the Absorber Layer on Performance Parameters. Defect density is another significant property that has a direct influence on the efficiency of solar cells. Defects regulate interfacial recombination rate, carrier lifetime, and material doping level.[35] The photogenerated current is mainly produced in the absorber layer. Therefore, as the defect density increases, carrier recombination also increases, reducing device efficiency. Intrinsic point defects in Sb_2Se_3 single crystal and solar cells are similar.[36] Three intrinsic defects are vacancy defects, interstitial defects, and antisite defects. Vacancy defects (V_{Se}, V_{Sb}) occur when Sb or Se atoms are missing from one of its sites. Both antimony vacancies (V_{Sb1}, V_{Sb2}) exhibit an acceptor nature and are present above the VBM. They have a high enthalpy of formation, which indicates that their concentration in the material will not matter.[36] Selenium vacancies have a low enthalpy of formation and are very deep donor defects.[36] Interstitial defects (Sb_i, Se_i) occur when an atom occupies an interstitial site in the crystal lattice. They are deep defects and will hardly impact the material's electronic conductivity.

Antisite defects (Se_{Sb}, Sb_{Se}) occur when Se atoms occupy Sb sites and vice versa. Sb_2Se_3 exhibits p-type conductivity due to an antisite defect, Sb_{Se}.[36] According to the first-principle calculation, antisite defects are dominant in Sb_2Se_3 due to its 1D structure.[37] Antisite Se_{Sb} is a deep donor defect, whereas Sb_{Se} is a shallow acceptor defect. VTD-fabricated Sb_2Se_3 has two hole traps at 0.48 and 0.71 eV above the valence band (VB) and an electron trap at 0.61 eV below the conduction band (CB). The hole trap at 0.48 and 0.71 eV is due to VSb and SeSb acceptor defects, respectively, while the electron trap at 0.61 eV is due to Sb_{Se} antisite donor defects.[8] Here, in this simulation, the effect of antisite defect density is investigated, and vacancy defects are not included, as they have a high enthalpy of formation and are less likely to happen.

3.4.1. Varying Donor Defect Densities. This simulation is based on considering only donor-type (Sb_{Se} antisite) defects in the Sb_2Se_3 layer, which are present at 0.61 eV below CB. Here, the donor defect concentration is changed from 10^{12} to 10^{17} cm^{-3}. Figure 6a,b shows that all of the parameters decrease with increasing defect concentration. An optimum value of 10^{13} cm^{-3} is obtained for determining the $I-V$ characteristics, where photovoltaic parameters are 0.64 V, 37.60 mA cm^{-2}, 82.09%, and 19.75% (able ST5).

https://doi.org/10.1021/acsomega.2c07211
ACS Omega 2023, 8, 1632−1642

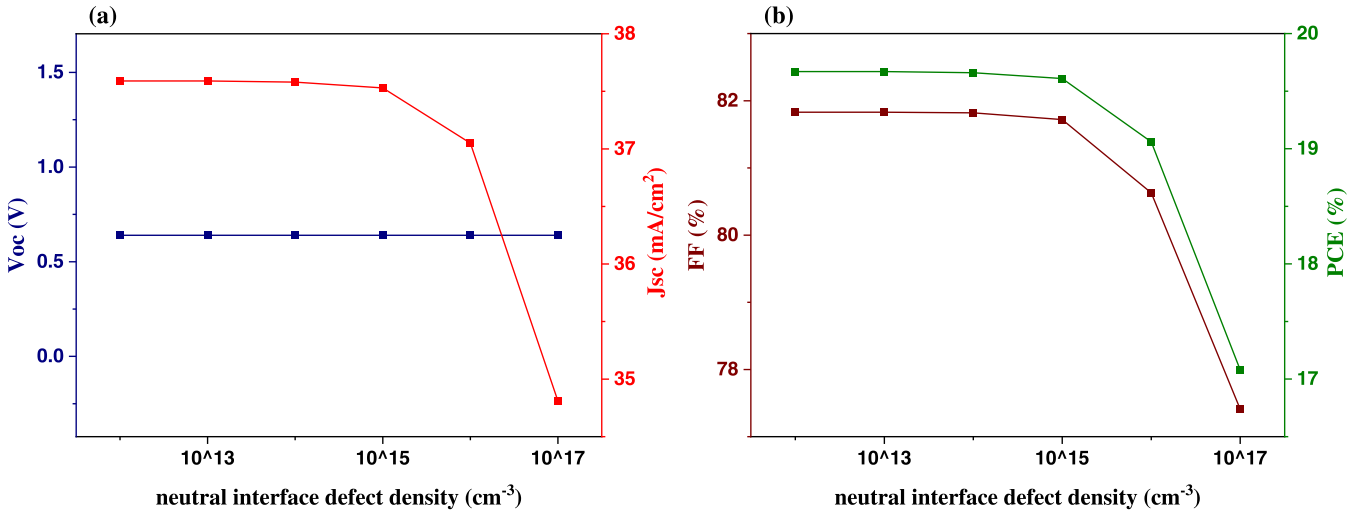

Figure 8. Variation of (a) V_{OC} and J_{SC} and (b) FF and PCE with neutral interface defect density.

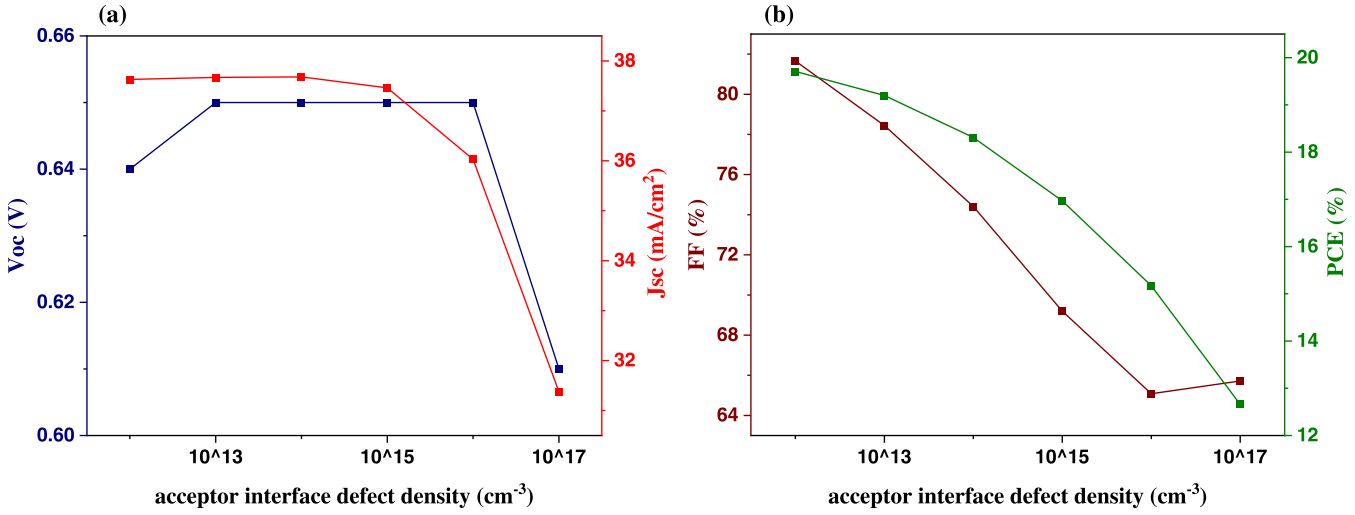

Figure 9. Variation of (a) V_{OC} and J_{SC} and (b) FF and PCE with acceptor interface defect density.

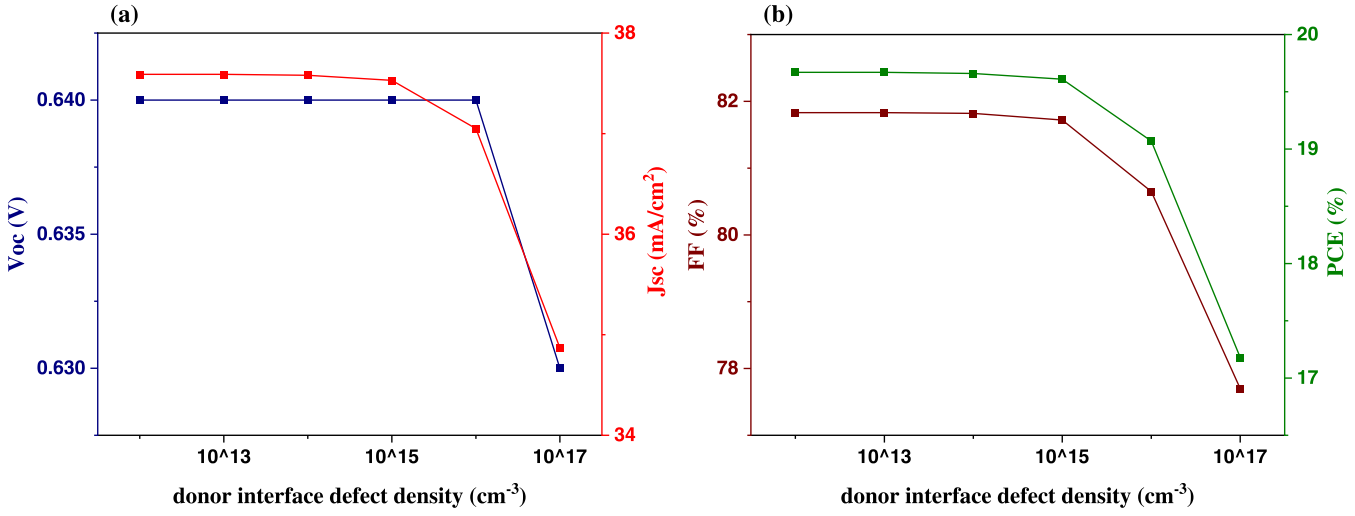

Figure 10. Variation of (a) V_{OC} and J_{SC} and (b) FF and PCE with donor interface defect density.

3.4.2. Varying Acceptor Defect Densities. Here, the simulation is carried out under consideration when the absorber layer contains only acceptor-type (Se_{Sb} antisite) defects at 0.71 eV above VB. It is seen from Figure 7a,b that when the defect density of the absorber layer is increased, FF and PCE decrease. In contrast, V_{OC} is constant at 0.64 V up to

https://doi.org/10.1021/acsomega.2c07211
ACS Omega 2023, 8, 1632−1642

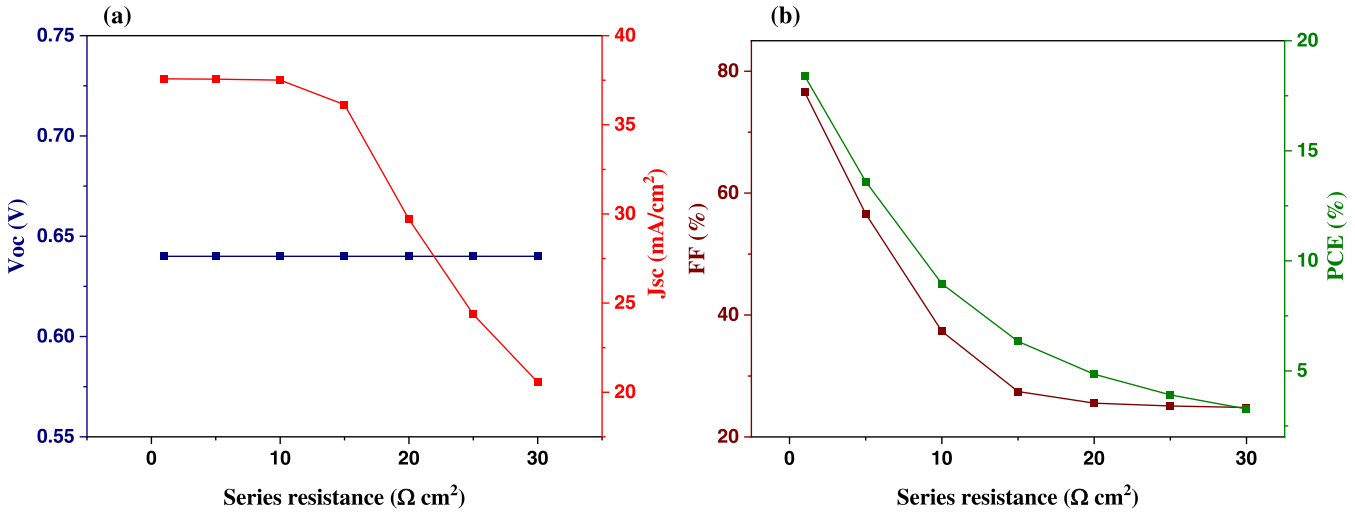

Figure 11. Variation of (a) V_{OC} and J_{SC} and (b) FF and PCE with series resistance.

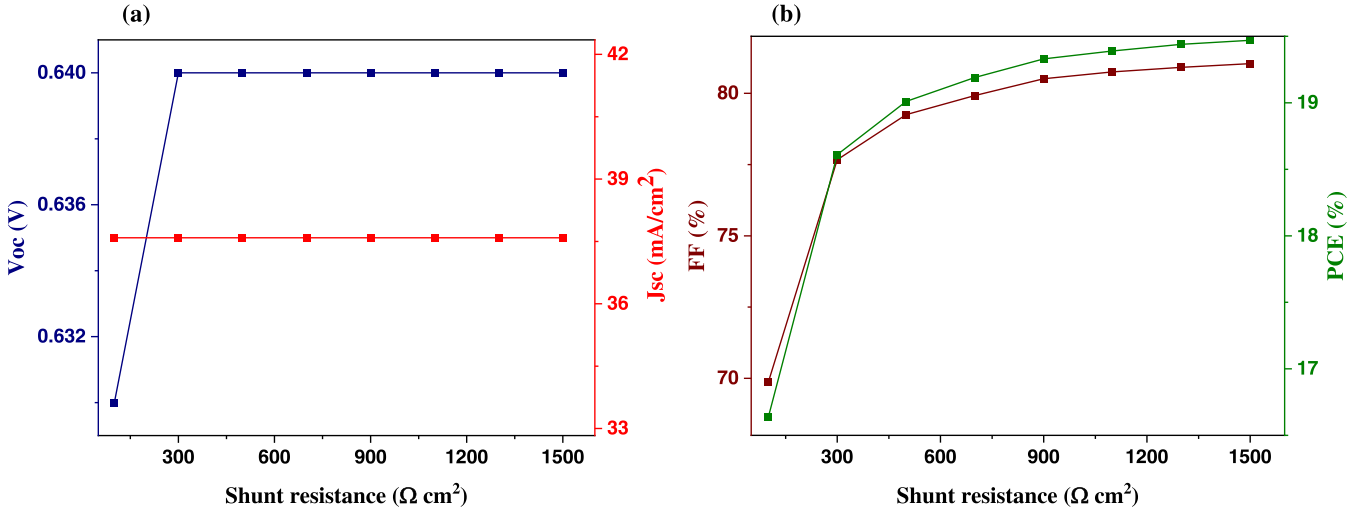

Figure 12. Variation of (a) V_{OC} and J_{SC} and (b) FF and PCE with shunt resistance.

10^{15} cm^{-3} concentration and then decreases, and J_{SC} remains constant at 37.60 mA cm^{-2} till 10^{13} cm^{-3} and then decreases. So, the optimum value of 10^{13} cm^{-3} is considered for the $I-V$ curve, where PCE, V_{OC}, FF, and J_{SC} are 19.75%, 0.64 V, 82.08%, and 37.60 mA cm^{-2} (Table S6), respectively.

There is a common observation in both types of defects that the device is defect tolerant up to 10^{15} cm^{-3} defect concentration, i.e., there is a very slight change in the values of photovoltaic parameters.

3.5. Influence of Varying Interface Defect Densities on PV Parameters. Interface states are a crucial factor that considerably affects solar cell performance. Sb_2Se_3 has an orthorhombic structure (unit cell parameters, a = 11.7808 Å, b = 3.9767 Å, c = 11.6311 Å), and ZnSe crystallizes in a hexagonal structure (unit cell parameters, $a = b = c$ = 5.668 Å). So, a lattice mismatch contributes to interface states and recombination. Interface recombination is one of the main reasons for the loss in V_{OC}, FF, and efficiency. At the ZnSe/Sb_2Se_3 interface, defect concentration is changed from 10^{12} to 10^{17} cm^{-3}.

3.5.1. Varying Neutral Defect Densities. It is seen in Figure 8a,b that with the increase in the concentration of neutral defects of the ZnSe/Sb_2Se_3 interface, the value of V_{OC} remains unaffected, but J_{SC}, FF, and PCE decrease with an increase in defect density (Table S7).

3.5.2. Varying Acceptor Defect Densities. It is seen in Figure 9a,b that with the increase in the concentration of acceptor defects, FF decreases by 20%, and PCE decreases by 37% for 10^{17} cm^{-3}. Still, there is a slight increase in V_{OC} and J_{SC} initially and then both decrease at higher defect concentrations (Table S8).

3.5.3. Varying Donor Defect Densities. It is seen from Figure 10a,b that there is a very minute change in J_{SC}, FF, and efficiency for donor defect concentration ranging from 10^{12} to 10^{15} cm^{-3}, while at a high defect concentration, there is a decrease in efficiency. J_{SC} changes by 7%, FF changes by 5%, and PCE changes by 12% from their respective values at 10^{12} cm^{-3}. It is observed that there is almost no effect on V_{OC} (1% decrease from the value at 10^{12} cm^{-3}; Table S9) with increasing donor defect concentration of the interface.

3.6. Influence of Varying Series and Shunt Resistances on PV Parameters. Series and shunt resistances are parasitic parameters that reduce the fill factor and, thus, solar cell efficiency. The metallic contacts and interconnections, carrier transit via the top diffused layer, the bulk resistance of the semiconductor material, and the contact resistance

https://doi.org/10.1021/acsomega.2c07211
ACS Omega 2023, 8, 1632−1642

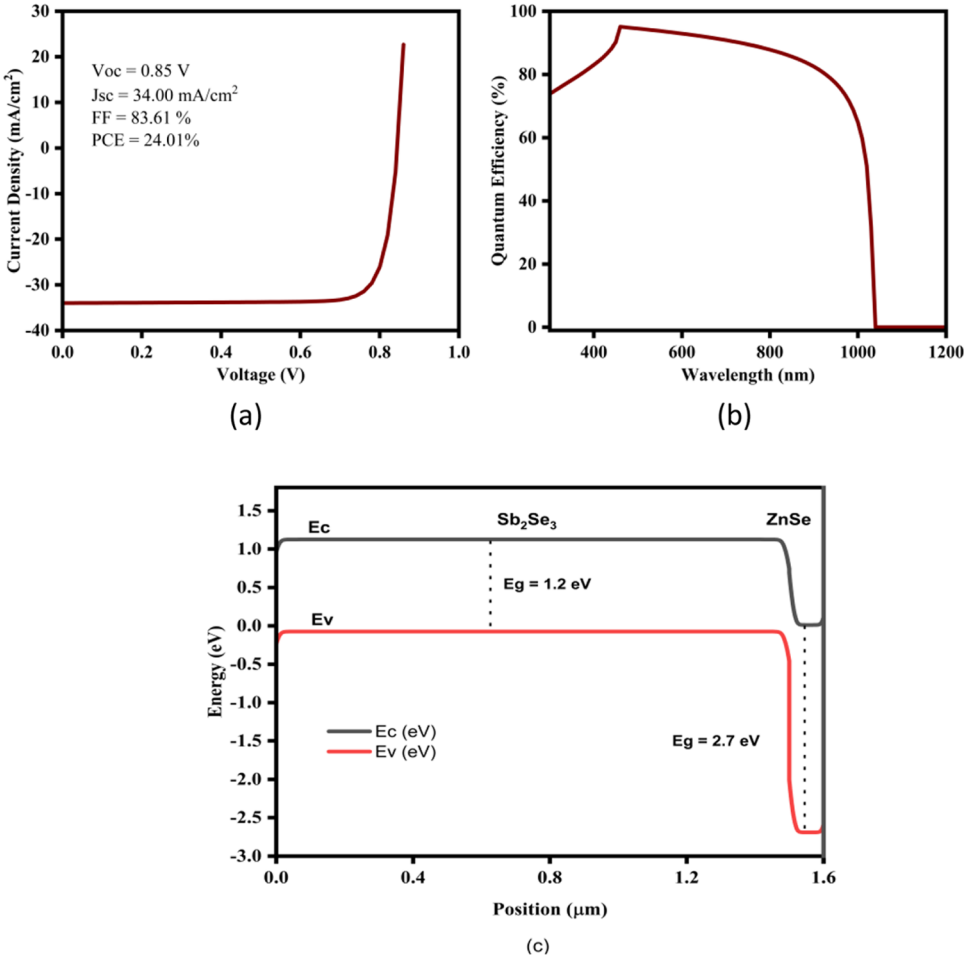

Figure 13. (a) $I-V$ curve, (b) EQE curve, (c) energy band diagram for the ZnSe/Sb_2Se_3 solar cell with optimized simulation parameters.

between semiconductor and metallic contacts significantly influence series resistance (R_s). The impurities and non-idealities decrease the shunt resistance (R_{sh}) at the p−n junction, which partially shortens the junction, especially close to cell boundaries.[38] In this study, R_s varies from 1.0 to 30 Ω cm^2, and R_{sh} ranges from 100 to 1500 Ω cm^2. From Figure 11a, it can be observed that V_{OC} remains unaffected at a value of 0.64 V (Table S10) with an increase in series resistance, and J_{SC} decreases abruptly after 15 Ω cm^2 to a value of 20.6 mA cm^{-2} at 30 Ω cm^2. Figure 11b shows that the FF value decreases from 76.53 to 37.34% with an increase in series resistance from 1 to 10 Ω cm^2. The efficiency decreases from 18.40 to 8.96% with an increase in series resistance from 1 to 10 Ω cm^2.

From Figure 12a,b, it is observed that with the increase in shunt resistance value, J_{SC} and V_{OC} remain constant at 37.59 mA cm^{-2} and 0.64 V, respectively. In contrast, FF and PCE increase rapidly to 77.67 and 18.61%, respectively, in the initial increase in shunt resistance and then increase slightly to reach maximum values of 81.04 and 19.47% at 1500 Ω cm^2 (Table S11), respectively. The low value of shunt resistance creates power losses in solar cells by giving the current generated by the light a short-circuit channel between the buffer and the metal. The voltage generated by the solar cell decreased due to this diversion. It also reduced the current flowing through the junction of the solar cell. The current density and the voltage at the maximum powerpoint decreased due to a reduction in FF. The optimized series and shunt resistance values are 1 and 1000 Ω cm^2, respectively.

3.7. Optimized Device Parameters, EQE Curve, and Energy Band Diagram. Figure 13a shows the $I-V$ curve under AM 1.5 G (1000 W m^{-2}, 300 K) illumination of the device with the optimized simulated parameters. The optimized parameters of the device are as follows: a 1.5 μm thin Sb_2Se_3 layer, a 0.1 μm thin ZnSe layer, 10^{18} cm^{-3} shallow acceptor density of the absorber layer, a recombination coefficient of 10^{-11} cm^3 s^{-1}, donor and acceptor defects of 10^{13} cm^{-3} concentration in the absorber layer, and a neutral interface defect of 10^{13} cm^{-3}. The maximum efficiency obtained for Sb_2Se_3/ZnSe solar cells using these optimized parameters is 24.0%. Other parameters of the device, such as V_{OC}, J_{SC}, and FF, are 0.85 V, 34 mA cm^{-2}, and 83.6%, respectively.

Figure 13b shows that the EQE covers the entire visible spectrum and has a strong spectral response between 300 and 1000 nm. Additionally, the ZnSe/Sb_2Se_3 solar cell converts more photons into charge carriers in the shorter wavelength region than the commonly used CdS buffer layer. The parasitic absorption of the CdS layer is responsible for reducing the shorter wavelength region.[34]

The energy band structure of the ZnSe/Sb_2Se_3 solar cell is shown in Figure 13c. When photogenerated carriers separate at the intersection of the buffer and absorber layers, the built-in voltage induced by the strong electric field of the p−n junction accelerates the charge carriers, causing them to be quickly

https://doi.org/10.1021/acsomega.2c07211
ACS Omega 2023, 8, 1632−1642

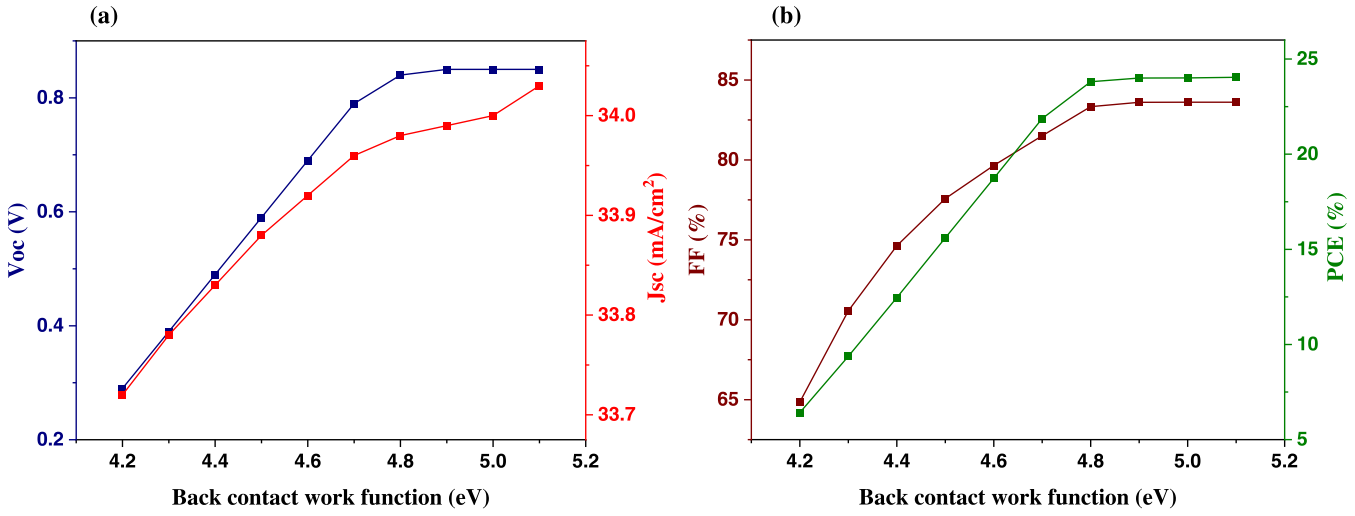

Figure 14. Variation of (a) V_{OC} and J_{SC} and (b) FF and PCE with the back contact work function.

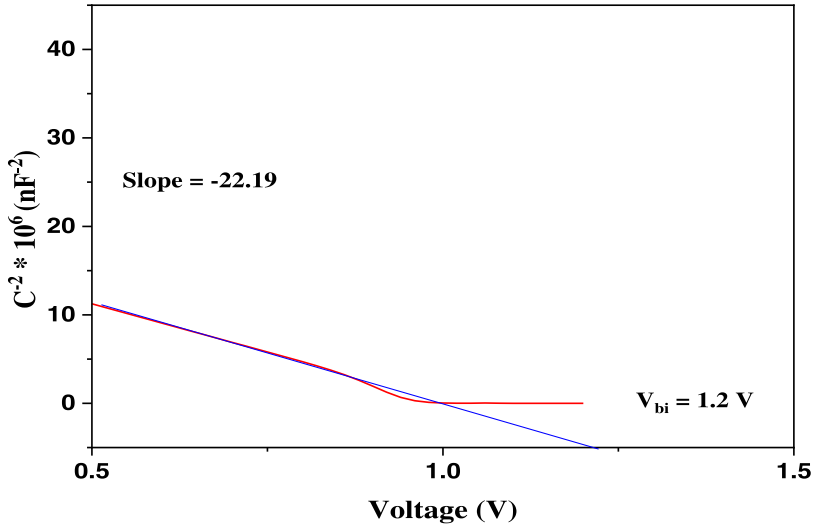

Figure 15. Mott−Schottky plot for the ZnSe/Sb_2Se_3 device.

drawn apart from the p−n junction. As the holes pass through the absorber layer and electrons through the buffer layer, they are collected by the back and front contacts, respectively. The charge carriers are well suited to the band offsets and can reach the metal contact without recombination.

3.8. Influence of Varying Rear Metal Work Functions on PV Parameters. Back contact functions as a contact for transferring carriers to the load and as an optical reflector. A variety of materials have been suggested as back contacts, such as aluminum (4.28 eV), silver (4.3 eV), tungsten (4.5 eV), copper (4.61 eV), molybdenum (5.0 eV), gold (5.1 eV), etc. Mo and Au are the most typical material utilized for the rear contact. It is due to the low contact resistance of molybdenum to the absorber layer and its stability at processing temperatures. These can reduce atom diffusion, minimizing harmful reactions during Sb_2Se_3 development.[39] Gold is an inert metal and does not have undesirable interfacial interactions with the absorber. Both Mo (5.0 eV) and Au (5.1 eV) metals have a high work function, which is necessary to avoid a high energy hurdle for hole extraction at the rear interface in absorbers of p-type conductivity and to produce an ohmic contact.[40] Here, the rear metal contact work function varies from 4.2 to 5.1 eV. Figure 14a shows that V_{OC} and J_{SC} increase (Table S12) as the back contact work function increases. Figure 14b illustrates that FF and PCE also increase gradually with the increase of back contact work function. It can be seen that when the value is below 4.8 eV, the solar cell's performance suffers significantly. It is due to the potential for the Schottky junction to form at the Sb_2Se_3/metal interface, which may happen due to Fermi-level pinning at the interface.[41] So, to achieve better device performance, the rear metal work function should be above 4.8 eV.

3.9. Capacitance−Voltage Characteristics. The $C-V$ studies are done to discover more fundamental characteristics of the solar device. The essential parameters generated from the capacitance−voltage curve are built-in potential (V_{bi}) and doping density (N_a), which are shown by the following two relations[42,43]

$$\frac{1}{C^2} = \frac{2}{qN_a\varepsilon_0\varepsilon_s A^2}(V_{bi} - V) \quad (5)$$

$$N_a = \frac{2}{q\varepsilon_0\varepsilon_s A^2\left[\frac{d}{dv}\left(\frac{1}{C^2}\right)\right]} \quad (6)$$

https://doi.org/10.1021/acsomega.2c07211
ACS Omega 2023, 8, 1632−1642

where C is the measured capacitance, q is the charge of an electron, N_a is the doping density, ε_0 is the permittivity of the free space (8.85×10^{-14} F cm^{-1}), ε_s is the dielectric constant, A is the area of the cell (1 cm^2), V_{bi} is the built-in potential, and V is the applied potential.

A linear area with a slope equal to the doping concentration is produced by eq 5. The cell's built-in voltage is obtained by the intersection of $1/C^2$ with the voltage axis, which is 1.2 V. The $C-V$ studies are done at a frequency of 1 MHz.

A Mott–Schottky plot, obtained from $C-V$ characteristics, is shown in Figure 15.

By putting all of the values of parameters and slope (−22.19) in eq 6, N_a is found to be 3.5×10^{17} cm^{-3}. Since the plot has a negative slope, it is likely that the majority of charge carriers are holes and that the p-type Sb_2Se_3 layer contains most of the space charge area. V_{bi} and N_a are much higher than those of CdS–Sb_2Se_3 heterojunction solar cells.[43,44]

4. CONCLUSIONS

In this study, SCAPS-1D was used to simulate the Mo/Sb_2Se_3/ZnSe/Al solar cell to obtain optimized parameters of the solar device. The solar cell's efficacy is tuned for various controllable factors, including the thickness of the buffer and absorber layers, acceptor density and defect, recombination, shunt and series resistance, and rear metal work function. Results show that other properties of the solar device, such as efficiency, are notably influenced by the absorber layer's thickness. The buffer and absorber layers' thicknesses are optimized to 100 nm and 1.5 μm, respectively. The RRC value obtained is 10^{-11} cm^3 s^{-1}. For Sb_2Se_3-based solar cells to work at their best, the simulation findings further highlighted the significance of managing radiative recombination, defect, and shallow acceptor density. The most outstanding efficiency for the ZnSe/Sb_2Se_3 solar cell after adjusting all of the parameters above is 24%. The Mott–Schottky plot showed that the built-in voltage of the device was 1.2 V, and the cell had a carrier concentration of 3.5×10^{17} cm^{-3}. The results of this study will help the researchers to develop highly efficient Sb-chalcogenide-based solar cells with less-toxic and earth-abundant materials.

■ ASSOCIATED CONTENT

Supporting Information

The Supporting Information is available free of charge at https://pubs.acs.org/doi/10.1021/acsomega.2c07211.

> Various tables presenting the influence of Sb_2Se_3 thickness; ZnSe thickness; Sb_2Se_3 shallow acceptor doping density; varying radiative recombination coefficients; varying donor defect densities of the Sb_2Se_3 layer; acceptor defect density of the Sb_2Se_3 layer; varying neutral interface defect densities of ZnSe/Sb_2Se_3; varying acceptor interface defect densities of ZnSe/Sb_2Se_3; varying donor interface defect densities of ZnSe/Sb_2Se_3; series resistance; varying shunt resistances; and varying back contact metal work function on device performance (PDF)

■ AUTHOR INFORMATION

Corresponding Author

Vidya Nand Singh − *Academy of Scientific and Innovative Research (AcSIR), Ghaziabad 201002, India; Indian Reference Materials (BND) Division, CSIR-National Physical Laboratory, New Delhi 110012, India;* orcid.org/0000-0002-4691-3142; Email: singhvn@nplindia.org

Authors

Raman Kumari − *Academy of Scientific and Innovative Research (AcSIR), Ghaziabad 201002, India; Indian Reference Materials (BND) Division, CSIR-National Physical Laboratory, New Delhi 110012, India*

Mamta Mamta − *Academy of Scientific and Innovative Research (AcSIR), Ghaziabad 201002, India; Indian Reference Materials (BND) Division, CSIR-National Physical Laboratory, New Delhi 110012, India*

Rahul Kumar − *Academy of Scientific and Innovative Research (AcSIR), Ghaziabad 201002, India; Indian Reference Materials (BND) Division, CSIR-National Physical Laboratory, New Delhi 110012, India*

Yogesh Singh − *Academy of Scientific and Innovative Research (AcSIR), Ghaziabad 201002, India; Indian Reference Materials (BND) Division, CSIR-National Physical Laboratory, New Delhi 110012, India*

Complete contact information is available at: https://pubs.acs.org/10.1021/acsomega.2c07211

Notes

The authors declare no competing financial interest.

■ ACKNOWLEDGMENTS

R. Kumari highly acknowledges University Grants Commission (UGC), India, for the Senior Research Fellowship (SRF) grant. Mamta, R. Kumar, and Y.S. highly acknowledge the Council for Scientific and Industrial Research (CSIR), India, for the Senior Research Fellowship (SRF) grant. The authors would like to thank their institute and Professor Burgelman of Gent University in Belgium, who provided SCAPS software.

■ REFERENCES

(1) Li, Z.; Liang, X.; Li, G.; Liu, H.; Zhang, H.; Guo, J.; Chen, J.; Shen, K.; San, X.; Yu, W.; Schropp, R.-E.-I.; Mai, Y. 9.2%-efficient core-shell structured antimony selenide nanorod array solar cells. *Nat. Commun.* **2019**, *10*, No. 125.

(2) Zhou, Y.; Leng, M.; Xia, Z.; Zhong, J.; Song, H.; Liu, X.; Yang, B.; Zhang, J.; Chen, J.; Zhou, K.; Han, J.; Cheng, Y.; Tang, J. Solution-processed antimony selenide heterojunction solar cells. *Adv. Energy Mater.* **2014**, *4*, No. 1301846.

(3) Wang, L.; Li, D.; Li, K.; Chen, C.; Deng, H.-X.; Gao, L.; Zhao, Y.; Jiang, F.; Li, L.; Huang, F.; He, Y.; Song, H.; Niu, G.; Tang, J. Stable 6%-efficient Sb_2Se_3 solar cells with a ZnO buffer layer. *Nat. Energy* **2017**, *2*, 17046.

(4) Chen, C.; Wang, L.; Gao, L.; Nam, D.; Li, D.; Li, K.; Zhao, Y.; Ge, C.; Cheong, H.; Liu, H.; Song, H.; Tang, J. 6.5% Certified efficiency Sb_2Se_3 solar cells using PbS colloidal quantum dot film as Hole-transporting layer. *ACS Energy Lett.* **2017**, *2*, 2125−2132.

(5) Chen, C.; Bobela, D.-C.; Yang, Y.; Lu, S.; Zeng, K.; Ge, C.; Yang, B.; Gao, L.; Zhao, Y.; Beard, M.-C.; Tang, J. Characterization of basic physical properties of Sb_2Se_3 and its relevance for photovoltaics. *Front. Optoelectron.* **2017**, *10*, 18−30.

(6) Messina, S.; Nair, M. T. S.; Nair, P. K. Antimony Selenide absorber thin films in all-chemically deposited solar cells. *J. Electrochem. Soc.* **2009**, *156*, H327−H332.

(7) Choi, Y.-C.; Mandal, T.-N.; Yang, W.-S.; Lee, Y.-H.; Im, S.-H.; Noh, J.-H.; Seok, S.-I. Sb_2Se_3-sensitized Inorganic-organic heterojunction solar cells fabricated using a single-source precursor. *Angew. Chem., Int. Ed.* **2014**, *53*, 1329−1333.

(8) Wen, X.; Chen, C.; Lu, S.; Li, K.; Kondrotas, R.; Zhao, Y.; Chen, W.; Gao, L.; Wang, C.; Zhang, J.; Niu, G.; Tang, J. Vapor transport

deposition of antimony selenide thin film solar cells with 7.6% efficiency. *Nat. Commun.* **2018**, *9*, No. 2179.
(9) Mamta, M.; Maurya, K.-K.; Singh, V.-N. Efficient Sb_2Se_3 solar cell with a higher fill factor: A theoretical approach based on thickness and temperature. *Sol. Energy* **2021**, *230*, 803−809.
(10) Ahmed, S.-R.-A.; Sunny, A.; Rahman, S. Performance enhancement of Sb_2Se_3 solar cell using a back surface field layer: A numerical simulation approach. *Sol. Energy Mater. Sol. Cells* **2021**, *221*, No. 110919.
(11) Baig, F.; Khattak, Y.-H.; Beg, S.; Soucase, B.-M. Numerical analysis of a novel CNT/Cu_2O/Sb_2Se_3/In_2S_3/ITO antimony selenide solar cell. *Optik* **2019**, *197*, No. 163107.
(12) Zhou, Y.; Wang, L.; Chen, S.; Qin, S.; Liu, X.; Chen, J.; Xue, D.-J.; Luo, M.; Cao, Y.; Cheng, Y.; Sargent, E.-H.; Tang, J. Thin-film Sb_2Se_3 photovoltaics with oriented one-dimensional ribbons and benign grain boundaries. *Nat. Photonics* **2015**, *9*, 409−415.
(13) Wang, Y.; Ji, S.; Shin, B. Interface engineering of antimony selenide solar cells: A review on the optimization of energy band alignments. *J. Phys. Energy* **2022**, *4*, No. 044002.
(14) Akin, S.; Arora, N.; Zakeeruddin, S.-M.; Grätzel, M.; Friend, R.-H.; Dar, M.-I. New strategies for defect passivation in high-efficiency Perovskite solar cells. *Adv. Energy Mater.* **2019**, *10*, No. 1903090.
(15) Godt, J.; Scheidig, F.; Siestrup, C.-G.; Esche, V.; Brandenburg, P.; Reich, A.; Groneberg, D.-A. The toxicity of Cadmium and resulting hazards for human health. *J. Occup. Med. Toxicol.* **2006**, *1*, No. 16961932.
(16) Totsch, W. Cadmium- towards a rational use of toxic element. *Environ. Manage.* **1990**, *14*, 333−338.
(17) Benavides, M.-P.; Gallego, S.-M.; Tomaro, M.-L. Cadmium toxicity in Plants. *Braz. J. Plant Physiol.* **2005**, *17*, 21−34.
(18) Mavlonov, A.; Razykov, T.; Raziq, F.; Gan, J.; Chantana, J.; Kawano, Y.; Nishimura, T.; Wei, H.; Zakutayev, A.; Minemoto, T.; Zu, X.; Li, S.; Qiao, L. A review of Sb_2Se_3 photovoltaic absorber materials and thin-film solar cells. *Sol. Energy* **2020**, *201*, 227−246.
(19) Li, G.; Li, Z.; Liang, X.; Guo, C.; Shen, K.; Mai, Y. Improvement in Sb_2Se_3 Solar cell efficiency through band alignment engineering at buffer/absorber interface. *ACS Appl. Mater. Interfaces* **2019**, *11*, 828−834.
(20) Mamta; Maurya, K.-K.; Singh, V.-N. Enhancing the performance of a Sb_2Se_3-based solar cell by dual buffer layer. *Sustainability* **2021**, *13*, 12320.
(21) Pathak, R. K.; Bais, S. ZnSe thin films- a brief review. *Int. J. Adv. Eng. Technol.* **2014**, *7*, 1300−1305.
(22) Oztas, M.; Bedir, M.; Bakkaloglu, O.-F.; Ormanci, R. Effect of Zn:Se ratios on the properties of sprayed ZnSe thin films. *Acta Phys. Pol. A* **2005**, *107*, 525−534.
(23) Lokhande, C.-D.; Patil, P.-S.; Tributsch, H.; Ennaoui, A. ZnSe thin films by Chemical Bath deposition method. *Sol. Energy Mater. Sol. Cells* **1998**, *55*, 379−393.
(24) Sayeed, M.-A.; Rouf, H.-K.; Hussain, K.-M.-A. Effect of thickness on characteristics of ZnSe thin film synthesized by vacuum thermal evaporation. *J. Theor. Appl. Phys.* **2020**, *14*, 251−259.
(25) Riveros, G.; Gomez, H.; Henriquez, R.; Schrebler, R.; Marotti, R.; Dalchiele, E.-A. Electrodeposition and characterization of ZnSe semiconductor thin films. *Sol. Energy Mater. Sol. Cells* **2001**, *70*, 255−268.
(26) Zandi, S.; Saxena, P.; Razaghi, M.; Gorji, N.-E. Simulation of CZTSSe thin-film solar cells in COMSOL: three-dimensional optical, electrical and thermal models. *IEEE J. Photovoltaics* **2020**, *10*, 1503−1507.
(27) Elbar, M.; Tobbeche, S. Numerical simulation of CGS/CIGS single and tandem thin-film solar cells using the Silvaco-Atlas software. *Energy Procedia* **2015**, *74*, 1220−1227.
(28) Mostefaoui, M.; Mazari, H.; Khelifi, S.; Bouraiou, A.; Dabou, R. Simulation of high efficiency CIGS solar cells with SCAPS-1D software. *Energy Procedia* **2015**, *74*, 736−744.
(29) Yaşar, S.; Kahraman, S.; Cetinkaya, S.; Apaydin, S.; Bilican, I.; Uluer, I. Numerical thickness optimization study of CIGS based solar cells with wxAMPS. *Optik* **2016**, *127*, 8827−8835.
(30) Sadek, M.-S.-I. Performance study of CZTS solar cell by optimizing buffer layer materials (ZnS and SnS) using AMPS-1D simulation. *SEU J. Sci. Eng.* **2019**, *13*, 30−35.
(31) Burgelman, M.; Decock, K.; Khelifi, S.; Abass, A. Advanced electrical simulation of thin-film solar cells. *Thin Solid Films* **2013**, *535*, 296−301.
(32) Li, Z.-Q.; Ni, M.; Fang, X.-D. Simulation of Sb_2Se_3 solar cell with a hole transport layer. *Mater. Res. Express* **2020**, *7*, No. 016416.
(33) Hossain, J. Design and simulation of double-heterojunction solar cells based on Si and GaAs wafers. *J. Phys. Commun.* **2021**, *5*, No. 085008.
(34) Lin, L.-Y.; Jiang, L.-Q.; Qiu, Y.; Fan, B.-D. Analysis of Sb_2Se_3/CdS based photovoltaic cell: A numerical simulation approach. *J. Phys. Chem. Solids* **2018**, *122*, 19−24.
(35) Hobson, T.-D.-C.; Phillips, L.-J.; Hutter, O.-S.; Durose, K.; Major, J.-D. Defect properties of Sb_2Se_3 thin film solar cells and bulk crystals. *Appl. Phys. Lett.* **2020**, *116*, No. 261101.
(36) Stoliaroff, A.; Lecomte, A.; Rubel, O.; Jobic, S.; Zhang, X.; Latouche, C.; Rocquefelte, X. Deciphering the role of key defects in Sb_2Se_3, a promising candidate for chalcogenide based solar cells. *ACS Appl. Energy Mater.* **2020**, *3*, 2496−2509.
(37) Liu, X.; Xiao, X.; Yang, Y.; Xue, D.-J.; Li, D.-B.; Chen, C.; Lu, S.; Gao, L.; He, Y.; Beard, M.-C.; Wang, G.; Chen, S.; Tang, J. Enhanced Sb_2Se_3 solar cell performance through theory-guided defect control. *Prog. Photovoltaics: Res. Appl.* **2017**, *25*, 861−870.
(38) The Behavior of Solar Cells, Chapter 3. https://www.eng.uc.edu/~beaucag/Classes/SolarPowerForAfrica/BookPartsPVTechnical/Behavior%20of%20PV_03.pdf.
(39) Ong, K. H.; Agileswari, R.; Maniscalco, B.; Arnou, P.; Kumar, C.-C.; Bowers, J.-W.; Marsadek, M.-B. Review on substrate and Molybdenum back contact in CIGS thin film solar cell. *Int. J. Photoenergy* **2018**, *2018*, No. 9106269.
(40) Zhang, J.; Kondrotas, R.; Lu, S.; Wang, C.; Chen, C.; Tang, J. Alternative back contacts for Sb_2Se_3 solar cells. *Sol. Energy* **2019**, *182*, 96−101.
(41) Gao, J.; Luther, J.-M.; Semonin, O.-E.; Ellingson, R.-J.; Nozik, A.-J.; Beard, M.-C. Quantum dot size dependent J-V characteristics in heterojunction ZnO/PbS quantum dot solar cells. *Nano Lett.* **2011**, *11*, 1002−1008.
(42) Tripathi, S.-K.; Sharma, M. Analysis of the forward and reverse bias I-V and C-V characteristics on Al/PVA:n-PbSe polymer nanocomposites Schottky diode. *J. Appl. Phys.* **2012**, *111*, No. 074513.
(43) Basak, A.; Singh, U.-P. Numerical modelling and analysis of earth abundant Sb_2S_3 and Sb_2Se_3 based solar cells using SCAPS-1D. *Sol. Energy Mater. Sol. Cells* **2021**, *230*, No. 111184.
(44) Yang, K.; Li, B.; Zeng, G. Effects of substrate temperature and SnO_2 high resistive layer on Sb_2Se_3 thin film solar cells prepared by pulsed layer deposition. *Sol. Energy Mater. Sol. Cells* **2020**, No. 110381.

https://doi.org/10.1021/acsomega.2c07211
ACS Omega 2023, 8, 1632−1642